ADVANCED OPTICAL MATERIALS
www.advopticalmat.de



# CW EPR Investigation of Red-Emitting CaS:Eu Phosphors: Rationalization of Local Electronic Structure

*Jacob N. Spencer,* Danielle Merrikin, Simon J. A. Pope, David J. Morgan, Nicholas Carthey, and Damien M. Murphy**

**A series of commercial and prepared CaS:$Eu^{2+}$ rare earth activated phosphors are investigated following different post-synthetic treatments. A number of species directly related to the function of the material are characterized using electron paramagnetic resonance (EPR) spectroscopy. Isolated $Eu^{2+}$ sites are identified and associated with the substitutional doping for $Ca^{2+}$ in the lattice which are responsible for the 645 nm emission of interest. Another inactive $Eu^{2+}$ site based within a "EuO" type phase aggregated on the surface of the material is also identified, as well as competitive $F^{+}$ center defects that are known to reduce emission from the $Eu^{2+}$ sites. Intrinsic $Mn^{2+}$ impurities are identified and used as local order probes to determine changes in ordering and symmetry upon cryo-milling and heating treatments of the samples. X-ray photoelectron (XPS) and photoluminescence (PL) spectroscopies are also conducted to complement the local structure observations. The reported data is useful in understanding how the nature of the lattice affects ground state electronic structure of functional defective sites, for the development of efficient and selective materials.**

## 1. Introduction

Rare earth activated phosphors have long been of interest owing to their efficient luminescent properties and tuneability, making them ideal materials for a variety of applications including optoelectronics,[1] solid state lighting,[2,3] persistent luminescence[4,5] and scintillation devices.[6–8] Phosphors are luminescent solids consisting primarily of a host lattice and a photoluminescent activator species, typically a 3d or 4f metal which is responsible for the functional role of the material. Commonly used 4f metal activators are lanthanides, including $Eu^{2+}/Eu^{3+}$, $Ce^{3+}$, $Tb^{3+}$, $Gd^{3+}$, $Yb^{3+}$, $Dy^{3+}$.[9] It is the unique electronic structure of the f-block elements that is responsible for their desirable catalytic, magnetic and photophysical properties.

These phosphors can be broadly classified into two groups, based on the desired electronic transition and emission band width required; namely, broad band 5d → 4f interelectronic transitions possessing a short radiative lifetime (cf. 1 µs) and sharp emission bands arising from 4f → 4f intraelectronic transitions, that are La-Porte forbidden, possessing a longer radiative lifetime (cf. 1 ms).[10] The 4f subshell is relatively insensitive to the local environment, due to the screening of occupied 5s and 5p subshells which reduce the electrostatic potential of the ligand field. Therefore, the sharp f–f band transitions are usually weakly affected by an external bias, although the relative intensities can be perturbed significantly. The relative energy and degeneracy of the 5d orbitals are in contrast significantly influenced by the crystal field. Consequently, the relative energy between the 4f and 5d states, and thus the corresponding emissive wavelength, is readily tuned by the coordination environment.

After the Coulombic and crystal field effects, other important considerations include dopant concentration, particle size distribution, crystallinity and concentration of defects or impurities within the material which may compete with the lanthanide activator. As a result, the specific luminescent intensity of the broad band may be reduced via interaction with these impurities, either by competition for incident optical absorption, energy transfer processes, or quenching of luminescent emission at the desired wavelength.[11,12] The luminescent efficiency of phosphors is also highly dependent on the relaxation properties of the activator during absorption and emission, i.e., the amount of energy lost to the lattice as heat,[9] which must be minimized to preserve the overall quantum yield.

$Eu^{2+}$-doped calcium sulfide (labeled hereafter as CaS:Eu) phosphors have in particular recently generated considerable interest as solid state light sources for algae growth, owing to the broad band red emission near $\lambda$ = 645 nm. Eu is readily found in the divalent oxidation state due to a half-filled 4f subshell and resulting stabilization energy. Over 300 $Eu^{2+}$ compounds in different host matrices have been reported to date, where the emission color of the 5d–4f transition has been tuned

J. N. Spencer, D. Merrikin, Prof. S. J. A. Pope, Dr. D. J. Morgan, Prof. D. M. Murphy
School of Chemistry
Cardiff University
Main Building, Park Place, Cardiff CF10 3AT, UK
E-mail: SpencerJ4@cardiff.ac.uk; MurphyDM@cardiff.ac.uk
Dr. N. Carthey
Johnson Matthey Technology Centre
Blounts Court Road, Sonning Common, Reading, Berkshire RG4 9NH, UK
The ORCID identification number(s) for the author(s) of this article can be found under https://doi.org/10.1002/adom.202001241.



**DOI: 10.1002/adom.202001241**

from near ultraviolet to deep red.[11] The CaS host lattice is an indirect bandgap semiconductor with $E_g = 4.43$ eV possessing a NaCl-type cubic structure.[13] $Eu^{2+}$ is thought to substitute into regular octahedral $Ca^{2+}$ sites, with six $S^{2-}$ anions coordinated to the center. Since the ionic radius of $Eu^{2+}$ is 1.17 Å (compared to 1.00 Å for $Ca^{2+}$),[14] substitution is not expected to cause a large distortion away from the high local symmetry environment.

Despite their desirable photoluminescent properties, and appreciable quantum yields in terms of their broad band emission near 645 nm, commercial CaS:Eu materials typically have a mean particle size which is too large for application as a light source, where they are typically incorporated into a film or coating. Therefore, an alternative synthetic route or appropriate post-synthesis treatment such as grinding, are necessary to reduce the mean particle size distribution. Clearly, due to the influence of particle size, morphology, and levels of defects or impurities on the photoluminescent properties of the material, the synthesis method and any subsequent treatments require careful consideration, since subtle changes in the experimental conditions can have a substantial effect on the final functional properties of the material. A number of studies have reported the presence of various intrinsic point defects in these alkaline earth sulfides,[12,15–18] such as $S^{2-}$ vacancies, which can act as shallow electron traps (≈0.26 eV) below the conduction band of CaS.[16] Other $S^{2-}$ vacancies, stabilized by $Ca^{2+}$ interstitial centers, were also evidenced by EPR and thermoluminescent measurements.[16] The specific luminescent intensity of the broad band emission near 645 nm may then potentially be reduced via interaction with these impurities.

Owing to the paramagnetic nature of the photoluminescent species, and also of the common impurities ($Mn^{2+}$, $Cr^{3+}$) and defects ($F^+$-centers) present in the material, electron paramagnetic resonance (EPR) spectroscopy is a highly versatile and informative method to characterize such materials.[19] The EPR derived spin Hamiltonian parameters of the likely defects and impurities present in the materials are well known,[12] and can be easily identified to elucidate structural information on the local environment. Furthermore, transition metals, such as $Mn^{2+}$, are highly sensitive to structure and disorder and can therefore be used as local order probes in the CaS lattice.[15] The magnetic resonance properties of lanthanides such as $Eu^{2+}$ are less well known, but their interest and utility is becoming more apparent.[4] EPR spectroscopy is therefore a useful tool to probe their identity, characterize their ground state electronic structure, relative concentrations, and local coordination environment within the system, and may provide a meaningful comparison to other characterization methods.

The aim of this study was to provide a detailed characterization of the important photoluminescent species in CaS:Eu phosphors following a series of synthetic steps, and post-synthetic treatments, including grinding and heating, using variable frequency continuous wave (CW) EPR, XPS, and photoluminescence spectroscopy. In particular, we wanted to explore the ground state electronic structure of the photoluminescent $Eu^{2+}$ species, and impurities such as $Mn^{2+}$ that may be used as structural probes, via zero field splitting (ZFS) interactions, where lower order interaction terms for S state ions are not susceptible to their local environment in this series of doped CaS:Eu samples. Furthermore, the effect of post-synthetic treatments is known to alter the properties of these material, but the process is not well understood, so we sought to examine this based on the variation in magnetic properties. In this study, a series of undoped samples were also characterized to identify the presence of deactivating $F^+$ center defects, and radicals related to oxidative processes upon treatment. Finally, comparative XPS and photoluminescence studies were performed to underpin the primary EPR investigations, supporting findings determining the nature of local $Eu^{2+}$ sites identified, and their resultant luminescent properties after various treatments.

## 2. Results and Discussion

### 2.1. Treatment of the EPR Spin Hamiltonian Parameters for $Eu^{2+}$ and $Mn^{2+}$

The two isotopically abundant forms of Eu are $^{151}$Eu and $^{153}$Eu ($I = 5/2$). They are present in almost equal quantities and possess significantly different magnetic moments ($\mu/\mu_N = 3.4717$ and 1.5324, respectively[20]), which has a marked influence on the magnitude of the isotropic hyperfine component. The ground state electronic structure of $Eu^{2+}$, $^8S_{7/2}$, is paramagnetic and therefore EPR active ($S = 7/2$). Since $Eu^{2+}$ has a half-filled 4f subshell, $L = 0$ and therefore in the ground state $J = S$. The analysis of the $Eu^{2+}$ signal can then be treated in terms of an effective spin-only contribution, so higher level treatment of the spin system is not necessary to account for the large orbital interaction (i.e., $g \sim g_e$). Since the 4f subshell is insensitive to the crystal field environment, the $g$ and hyperfine values are not expected to vary significantly. On the other hand, $Eu^{3+}$ has a singlet $^7F_0$ ground state and is therefore EPR silent ($J = 0$) as higher $J$ states are typically well separated by zero field splitting (ZFS) in non-Kramers (integer spin) systems.[21]

Although the ground state of $Eu^{2+}$ is $^8S_{7/2}$, and is therefore insensitive to crystal field effects, the $4f^65d^1$ configuration of $Eu^{2+}$ is far more susceptible to Coulombic and crystal field interactions, due to the d-orbital degeneracy, which is lifted by interaction with the local ligand environment.[22] The first excited $4f^65d^1$ and $4f^7$ states ($^6P_{7/2}$) are significantly higher in energy and therefore relaxation back to the ground state is fast and not expected to contribute significantly to the EPR spectra. The magnitude of the isotropic hyperfine, $|A_{iso}|$, is reported to be ≈91 and 40 MHz for $^{151}Eu^{2+}$ and $^{153}Eu^{2+}$ respectively,[12] with corresponding $g_{iso} = 1.9913$ for both isotopes.

The spin Hamiltonian parameters for $Eu^{2+}$ and $Mn^{2+}$ centers observed in the EPR spectra of CaS:$Eu^{2+}$ samples reported here were calculated according to a spin Hamiltonian of the form:

$$\hat{H} = g\mu_B \vec{B}\cdot\vec{S} + A\cdot\vec{S}\cdot\vec{I} + \hat{H}_{ZFS} \quad (1)$$

where $g$ and $A$ are the $g$- and $A$-tensors, $\mu_B$ is the Bohr magneton, $\vec{B}$ is the external magnetic field and $\vec{S}$, $\vec{I}$ are the electron and nuclear spin operators, respectively. The $g$- and $A$-tensors were to first order assumed to be isotropic due to the cubic symmetry reasonable for S state ions such as $Eu^{2+}$.[21] In fact, non-isotropic $g$-tensor values are rarely observed within experimental error for S ground state ions.[23] The ZFS interaction is therefore a much more useful indicator of local site symmetry. For the other observed centers, not associated with transition

or lanthanide metals, the spin Hamiltonian in Equation (1) was used in the absence of the zero-field splitting (ZFS) term. The line shape of high spin $Mn^{2+}$ ($S = 5/2$) was indicative of cubic symmetry fine structure, as has been observed previously,[15] therefore the upper limit for the magnitude for the ZFS Hamiltonian term was estimated, which was poorly resolved within the experimentally observed linewidth. For the high spin systems ($Eu^{2+}$, $Mn^{2+}$), the ZFS Hamiltonian, $\widehat{H}_{ZFS}$, was characterized in terms of extended Stevens operators of fourth- ($S \geq 2$) and sixth-order ($S \geq 3$), as described by Abragam and Bleaney.[23] The second-order operators, which relate to the more traditional $D$ and $E$ terms, vanish for cubic symmetry giving a simpler spin Hamiltonian of the following form, related to a fourfold axis:

$$\widehat{H}_{ZFS} = \frac{b_4}{60}\left(O_4^0 + 5O_4^4\right) + \frac{b_6}{1260}\left(O_6^0 - 21O_6^4\right) \quad (2)$$

where $O_k^q$ are the extended spin operators,[23] and $b_k^q$ are ZFS parameters for the fourth- and sixth-order terms. The ZFS Hamiltonian for cubic $Mn^{2+}$ site is identical to the first part of equation 2, considering only the fourth-order terms. The orientation of the principle axes of the higher order ZFS terms, which are anisotropic and therefore angularly dependent, were assumed to be coincident with the molecular axes.

For lower symmetry sites bearing high spin systems, the ZFS Hamiltonian also includes second order ($k = 2$) terms, relating to two-fold axis symmetry operators as given in Equation (3), which are related to the traditional ZFS terms $D$ and $E$, Equation (4):

$$\widehat{H}_{ZFS} = \frac{b_2}{3}\left(O_2^0 + O_2^2\right) + \frac{b_4}{60}\left(O_4^0 + O_4^2 + O_4^4\right) + \frac{b_6}{1260}\left(O_6^0 + O_6^2 + O_6^4\right) \quad (3)$$

$$D = b_2^0 \; ; \; 3E = b_2^2 \quad (4)$$

Typically, the second-order terms are much larger in magnitude and therefore the fourth and sixth order terms become less significant. In order to extract and resolve all ZFS parameters, it becomes necessary to perform single-crystal studies as a function of orientation, which has not been reported. The magnitude of the sixth order terms have thus been neglected in the simulation approach. Moreover, the relative sign of the ZFS terms is difficult to determine above 77 K and the parameters reported are therefore magnitudes rather than absolute values. In most cases, the traditional inhomogeneous linewidths from distributions in $g$, $A$, or $D$ were acceptable to characterize line shapes in the spectra. However, for the cubic $Eu^{2+}$ and $Mn^{2+}$ sites, characterization of line strains in the spectra were expressed in terms of a homogeneous peak-to-peak linewidth, and a Gaussian distribution of the $b_4$ terms which are largest in magnitude, since the traditional strains of $g$, $A$, or $D$ were inappropriate under the proposed conditions. It is expected that small perturbations from cubic symmetry would have a dominating effect on the $b_4$ term, unless the distortions were severe enough to reintroduce significant $b_2$ terms, in which case the cubic ZFS Hamiltonian would also be inappropriate. Since the observed fine structure is relatively weakly resolved, typical for a powder spectrum, it is challenging to separate the distribution of individual $b_4$ terms without appropriate single crystal measurements. A Gaussian distribution with the same FWHM was therefore assumed in both $b_4^0$ and $b_4^4$, to further simplify the model. For the undoped samples, where multiple cubic $Mn^{2+}$ sites were observed, the fine structure is completely unresolved and therefore the line shape was approximated with a homogeneous Lorentzian line shape. This was suitable to extract the $g_{iso}$ and $A_{iso}$ values used to distinguish between the hosting phases.

### 2.2. CW X-Band (9 GHz) EPR Spectra of Commercial CaS:Eu Phosphors

The first series of samples (hereafter labelled CaSEu_1,2,3) analyzed in this study were based on a commercially available material, investigated in its native as-received form (CaSEu_1), and after further treatments including cryo-milling (CaSEu_2), and thermal treatment in air (CaSEu_3). The EPR measurements were undertaken in order to identify the presence of any point defects, to monitor the changes in local environment of the structural paramagnetic probes ($Mn^{2+}$) and most importantly to analyze the profile of the $Eu^{2+}$ signals. Due to the number of defective centers, Kröger-Vink notation will be defined and referred to for the distinct sites characterized in the studies. The resulting low temperature CW X-band (9 GHz) EPR spectra are shown in **Figure 1**. An additional figure presenting the separated $Mn^{2+}$ and $Eu^{2+}$ simulations for CaSEu_2 and CaSEu_3 can be found in Figure S1 (Supporting Information).

The spectra represent a composite and overlapping pattern from multiple paramagnetic centers. In the native sample, CaSEu_1 (Figure 1a), the two prominent $Eu^{2+}$ isotopes are clearly visible, with hyperfine values of $|A_{iso}| = 91$ MHz and $|A_{iso}| = 40.2$ MHz for $^{151}Eu^{2+}$ and $^{153}Eu^{2+}$ respectively, and with $g_{iso} = 1.9912$ in both cases. The extracted parameters are almost identical to those reported previously in the literature,[15] and are indicative of $Eu^{2+}$ centers in a nearly cubic site, with only a small degree of local symmetry distortion. This is consistent with the proposal of a well-isolated $Eu^{2+}$ ion, substitutionally exchanged for $Ca^{2+}$ in the cubic unit cell, in Kröger-Vink notation $Eu_{Ca}^{X}$. The intrinsic linewidth is relatively narrow, and hence the phase memory time, $T_m$, is expected to be slow, on the order of μs as evidenced by pulsed EPR measurements (Figure S2, Supporting Information). There is no clear evidence of any $Mn^{2+}$ signal initially present in the native sample, in contrast to previous reports.[12,15] A magnified view of the low field $|m_I| = 5/2$ signal is provided in Figure S3 (Supporting Information) for reference.

By comparison, the EPR spectra of the treated CaSEu_2 and CaSEu_3 samples (Figure 1b,c) show additional features that can be readily assigned to a high spin $Mn^{2+}$ center ($S = 5/2$, $I = 5/2$), denoted $Mn_{Ca}^{X}$. This $Mn^{2+}$ signal is characterized by $g_{iso} = 2.0021$ and $A_{iso} = 234$ MHz, which is consistent with those expected for $Mn^{2+}$ located in the CaS lattice at a regular octahedral substitutional $Ca^{2+}$ site.[12] The fact that this signal is not observable in the "as received" native sample, CaSEu_1 (Figure 1a), indicates a broadening of the intrinsic linewidth, and reduction in the $Eu^{2+}$ signal intensity following cryo-milling due to oxidation, which prevented the observation of the weaker $Mn^{2+}$ signals. Oxidative processes, following cryo-milling, have been indicated in EPR measurements of undoped samples, the systematic cryo-milling study, and luminescence measurements vide supra. It is possible that some trace contamination from the milling process could also contribute, but this is not expected to be the sole reason due to the considerable concentration. Fine structure arising

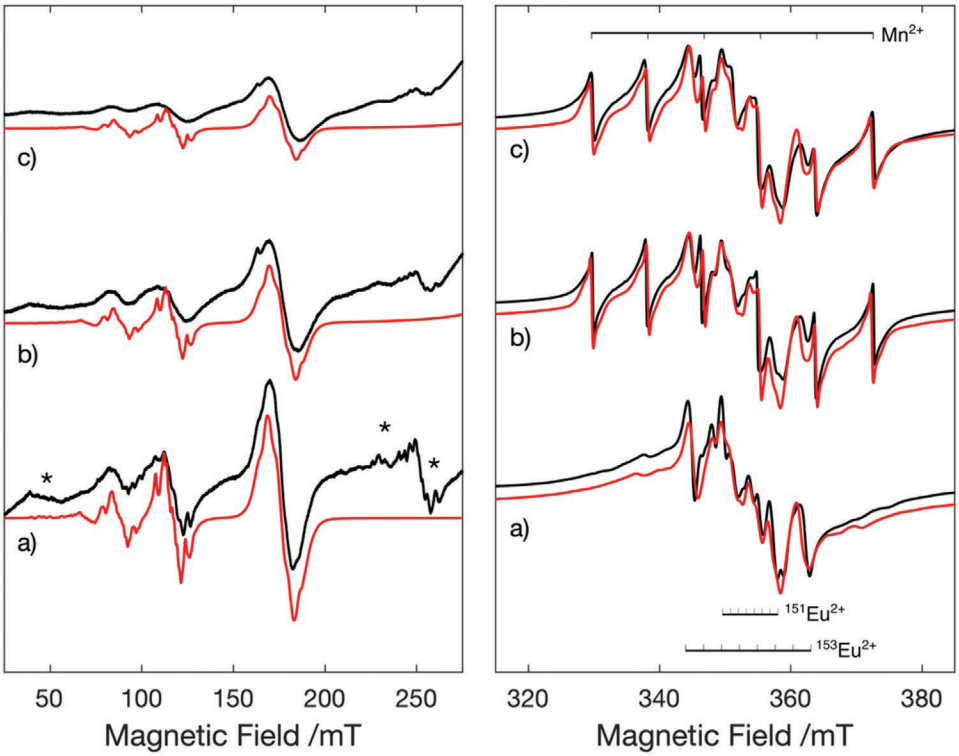


**Figure 1.** CW X-band (9 GHz) EPR spectra (120 K) of a) CaSEu_1, b) CaSEu_2 and c) CaSEu_3 samples. Left: low field measurement indicating the formally forbidden fine structure transitions. The asterisks indicate fine structure features not reproduced in the simulation of the cubic site $Eu^{x}_{Ca}$ species, and instead relate to the low symmetry $Eu^{x}_{surface}$ species (see Figure S7 in the Supporting Information). Right: high resolution spectra of the prominent features centered near $g_e$, including the $^{151,153}Eu^{2+}$ and $Mn^{2+}$ hyperfine patterns. An additional figure (Figure S1, Supporting Information), showing the deconvoluted simulations of $Eu^{x}_{Ca}$ and $Mn^{x}_{Ca}$ for CaSEu_2 and CaSEu_3 has been provided for clarity.

from the spin-spin interactions of $Mn^{2+}$ ($S = 5/2$) is noticeable (Figure S3, Supporting Information), indicating some disorder around the $Mn^{x}_{Ca}$ center due to vacancies and dislocations.[12] The accumulation of these effects are expected to be responsible for the decreased luminescence observed from the treated sample.

A noticeable difference in spectral linewidth is also observed for the $Mn^{x}_{Ca}$ centers after thermal treatment in air, namely for sample CaSEu_3 (Figure 1c). Since inhomogeneous broadening due to the suppressed fine structure does not directly broaden the central ($|\Delta m_s| = +1/2 \leftrightarrow -1/2$) transition, due to the non-degenerate interaction of the Kramers doublets ($|m_s| = 1/2, 3/2, 5/2$), this is instead attributed to a decrease in relaxation time, $T_2$, and therefore a change in local environment that broadens the intrinsic linewidth, vide infra. No other notable features are observed within this region, such as the expected $V_S^{\bullet}$ centers, metal impurities or additional sulfur radical species.

In the low magnetic field region of the EPR spectrum (Figure 1), another complex signal is observed for the samples which has not been previously reported in the literature, which corresponds to $Eu^{2+}$ fine structures. The simulated fine structure pattern is related to the cubic symmetry site with fourth and sixth-order ZFS terms. The fine structure patterns that do not appear in the simulation indicate the observation of another $Eu^{2+}$ environment occupying a lower symmetry site, which was resolved by comparison with the higher frequency W-band EPR measurement discussed later. The ZFS parameter values for this species are reported in **Table 1**. The corresponding spin Hamiltonian parameters obtained from simulations may be found in **Table 2**. The relative abundance of this second $Eu^{2+}$

**Table 1.** Experimental ZFS spin Hamiltonian parameters for $Eu^{2+}$ and $Mn^{2+}$ species identified in the CaS:Eu samples (Note: All $b_k^q$ parameters were determined by least-squares fitting procedures and are reported in MHz. The absolute sign of the parameters was not determined and therefore the magnitude of values is reported. The additional spin Hamiltonian parameters used in the simulation are given in Table 2).

| Species | | $b_2^0$ | $b_2^2$ | $b_4^0$ | $b_4^2$ | $b_4^4$ | $b_6^0$ | $b_6^2$ | $b_6^4$ |
|---|---|---|---|---|---|---|---|---|---|
| $Eu^{x}_{Ca}$ | Isolated (CaS)[c] | – | – | 47.1 | – | 235.3 | 16.0 | – | –336.0[a] |
| $Eu^{x}_{surface}$ | Surface ("EuO") | 2442.7 | 416.3 | 37.8 | –184.4[a] | 51.4 | N.R.[b] | N.R.[b] | N.R.[b] |
| $Mn^{x}_{Ca}$ (1) | Isolated | – | – | 12.6 | – | 63.0 | – | – | – |

[a]The negative sign denotes an opposite relative sign to the additional ZFS parameters, not an absolute sign; [b]Not resolved due to the magnitude of the $b_2$ and $b_4$ terms; [c]These values were obtained by simultaneous fitting of the X- and W-band spectra.

**Table 2.** Experimental *g* and *A* spin Hamiltonian parameters for the paramagnetic species observed in doped and undoped CaS samples (Note: All *A* values reported in MHz).

| Species | | $g_1$[a)] | $g_2$[a)] | $g_3$[a)] | $\|A_{iso}\|$[b)] |
|---|---|---|---|---|---|
| $Eu^{X}_{Ca}$ (CaS)[c)] | Isolated | 1.9912 | 1.9912 | 1.9912 | 40.2 |
| $Eu^{X}_{surface}$ | Surface ("EuO") | 1.9921 | 1.9921 | 1.9921 | 41.0[d)] |
| $Mn^{X}_{Ca}$ (1) | CaS | 2.0021 | 2.0021 | 2.0021 | 239.6 |
| $Mn^{X}_{Ca}$ (2) | CaO | 2.0015 | 2.0015 | 2.0015 | 254.5 |
| $V_S^{\cdot}$ | | 2.0031 | 2.0031 | 2.0031 | – |
| $S_xO_y^-$ radicals | $S_2O^-$ | 2.0035 | 2.0129 | 2.0328 | – |
| | $S_2O_2^-$ | 2.0045 | 2.0334 | 2.0529 | – |
| | $SO_2^-$ | 2.0030 | 2.0030 | 2.0125 | – |
| | $SO_3^-$ | 2.0049 | 2.0065 | 2.0063 | – |

[a)]±0.003; [b)]±5 MHz; For $Eu^{2+}$, the hyperfine values are quoted for major isotope $^{151}Eu$. Hyperfine values for $^{153}Eu$ correspond to $A(^{151}Eu)$ multiplied by the ratio of nuclear *g* factors $g_n$ for the isotopes ≈2.26 giving 91 MHz; [c)]These values were obtained by simultaneous fitting of the X- and W-band spectra; [d)]Hyperfine structure not resolved, assumed to be the same as for isolated species.

environment compared to the main $Eu^{X}_{Ca}$ signal observed at center field, 335 mT, is considerably smaller (<1:10), and may be responsible for part of the unresolved features to low and high field of the isolated $Eu^{X}_{Ca}$ hyperfine pattern.

### 2.3. CW W-Band (95 GHz) Spectra of Commercial and Prepared CaS:Eu Phosphors

In order to improve the resolution of the comparatively larger ZFS arising from this second $Eu^{2+}$ species in a lower symmetry environment, CW W-band (95 GHz) EPR spectra were recorded (**Figure 2**). When the ZFS parameters are comparable to or larger than the microwave quanta, complex EPR spectra are observed, which can be very difficult to accurately rationalize due to the presence of formally forbidden transitions.[24] When *D* (or higher order terms) << *hv*, all allowed transitions are possible and a fine structure pattern is observed from transitions between the respective Kramers doublets. Simulation of the resulting spectrum readily allows simulation of the ZFS parameters thus providing an informative view of the symmetry environment. A number of transitions are observed in the low field region of the X-band spectrum. Higher frequency measurements aid in resolving this structure and can also improve field resolution to assist in deconvolving the signals appearing at similar *g* values. A comparison of the W-band CW EPR spectra for the native commercial sample, CaSEu_1, and another sample prepared by a solid-state reduction synthesis method, labelled CaSEu_SSR, are shown in Figure 2. The signal intensities have been normalized for ease of comparison. A further magnified comparison of the experimental and simulated hyperfine pattern can be found in Figure S4 (Supporting Information).

With respect to the CaSEu_SSR sample, the hyperfine structure associated with the high symmetry $Eu^{X}_{Ca}$ environment, which is clearly visible in CaSEu_1 (Figure 2, left hand side), is now barely perceptible, buried within the most intense central peak pertaining to the $m_s = -1/2 \leftrightarrow +1/2$ transition. The resolution of this signal is obscured by the dominant fine structure in the spectrum, which is also observed in the X-band spectra for these samples (see Figures S5 and S6, Supporting Information for the X-band spectra of CaSEu_SSR), with estimated ZFS values reported in Table 1.

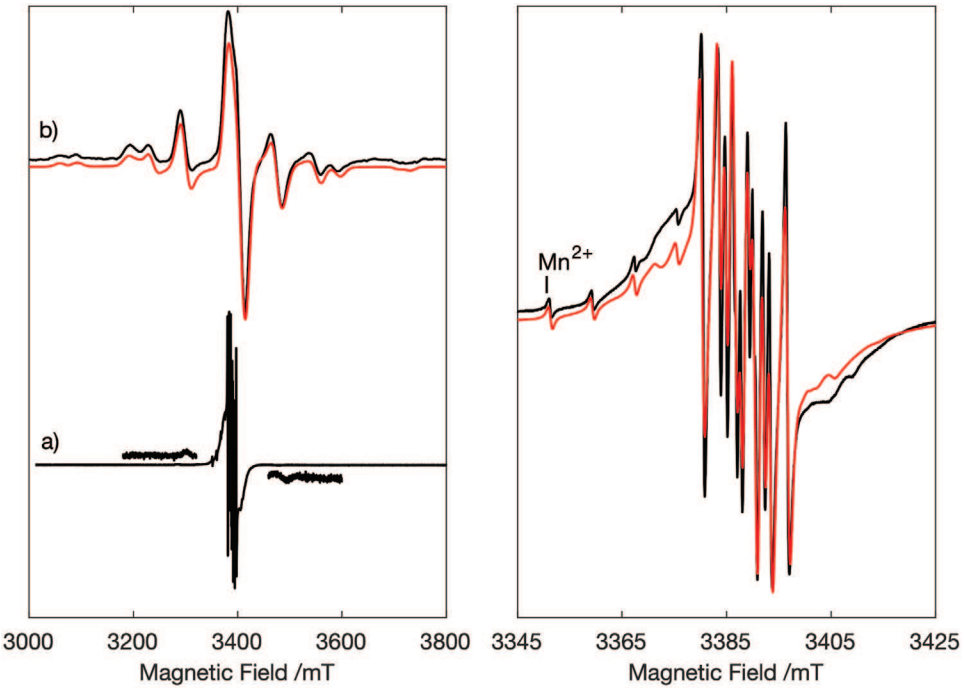


**Figure 2.** Left: Comparative CW W-band (95 GHz) EPR spectra (300 K) of a) the native commercial sample CaSEu_1, and b) sample prepared by solid-state reduction synthesis method, labeled CaSEu_SSR. Right: High-resolution spectrum of the native CaSEu_1 sample in (a). Black: experimental spectrum; Red: simulated spectrum.

This additional structure is a clear indication of the second low symmetry $Eu^{2+}$ environment suggested earlier, denoted as $Eu^{X}_{surface}$. In the commercial sample, CaSEu_1, very weak shoulders to low and high field of the central resonance indicates that this lower symmetry environment is also present here, albeit in much lower concentration. By simulation of the $Eu^{X}_{surface}$ species at X-band, using the spin Hamiltonian parameters obtained from fitting at W-band, the forbidden fine structure transitions in the low field region not reproduced by the $Eu^{X}_{Ca}$ simulation (Figure 1, left, denoted by asterisks) are now simulated reasonably well (see Figure S7 in the Supporting Information). Finally, the $Mn^{2+}$ hyperfine pattern which was not observed in CaSEu_1, is now resolved from the $Eu^{X}_{Ca}$ signal at higher frequency, indicating the presence of the high symmetry octahedral $Mn^{2+}$ species $Mn^{x}_{Ca}$ (1).

### 2.4. CW X-Band EPR of Prepared Undoped CaS Phosphors

In order to detect the presence of any underlying defect signals within the material, but which are not visible owing to the intense Eu signals, a series of undoped CaS samples were also analyzed. In the native undoped sample, the presence of multiple $S_xO_y^-$ type radicals can be clearly detected (**Figure 3**a). These species are presumably formed as by-products from the partial oxidation of CaS $\rightarrow CaSO_4$. Further analysis of the EPR spectra reveals the presence of two distinct sulfur based radicals, specifically assigned to $S_2O^-$ and $S_2O_2^-$ centers (see Figure S8 in the Supporting Information for details of the simulations).[25] The spin Hamiltonian parameters (Table 1) for these two sulfur radicals are slightly different compared to those reported previously in CaS powders,[15] and this may be an artefact of the different synthesis methods employed. No sharp isotropic signal due to any $V_S^{\bullet}$ centers were observed, which could indicate that such species are stabilized by cationic $Eu^{3+}$ defects, $Eu^{\bullet}_{Ca}$, as suggested in previous EPR studies.[15]

After heating this sample in an $N_2/H_2$ atmosphere, a complete loss of signals associated with the $S_xO_y^-$ radicals is observed, indicating a reduction of $S_xO_y^-$ to $S_x^-$ species in the highly reducing atmosphere (Figure 3b). Simultaneously, two new signals become visible in the spectrum, including a sharp isotropic signal which can be easily attributed to an $F^+$ center, $V_S^{\bullet}$, as well as the clear features arising from two distinct $Mn^{2+}$ species in an approximate 1:2 intensity ratio. In this case, a simpler line broadening model with a homogeneous Lorentzian linewidth was sufficient to reproduce the Mn signals. The hyperfine values for these $Mn^{X}_{Ca}$ species ($^{Mn(1)}A_{iso}$ = 239.6 MHz and $^{Mn(2)}A_{iso}$ = 254.5 MHz) are consistent with the known values reported for $Mn^{2+}$ embedded within a CaS and CaO phase respectively.[12,26] This indicates the presence of a CaO phase in the sample, formed through oxidation of the sample during synthesis. The slightly larger $A_{iso}$ value for the $Mn^{X}_{Ca}$(2) center is expected to result from the increased covalency in CaO due to the crystal field effect of $O^{2-}$ versus $S^{2-}$. No fine structure is resolved for $Mn^{2+}$ in this case, around the two isolated $Mn^{2+}$ environments, $Mn^{x}_{Ca}$(1) and $Mn^{X}_{Ca}$(2), and the six-line pattern is due to a hyperfine interaction with the nuclear dipole of $Mn^{2+}$ ($I$ = 5/2). It is expected that $Mn^{2+}$ would occupy similar cubic sites to $Eu^{2+}$ in the CaS lattice,[27] $Mn^{x}_{Ca}$(1), and also in the CaO phase,[26] $Mn^{x}_{Ca}$(2), i.e., in octahedral substitutional sites replacing $Ca^{2+}$. Therefore, these different $Mn^{2+}$ signals may indirectly evidence the possibility of two $Eu^{2+}$ environments, in CaS and CaO phases, although their spin Hamiltonian parameters are unlikely to vary significantly to be resolved from one another due to screening of the 4f ground state electrons.

Finally, after annealing and cryo-milling of the sample, little additional change can be seen in the spectrum (Figure 3c). A weak signal associated with the $S_xO_y^-$ species is visible, indicating that mechanical stress, induced by cryo-milling, can readily oxidize some of the diamagnetic sulfur radicals

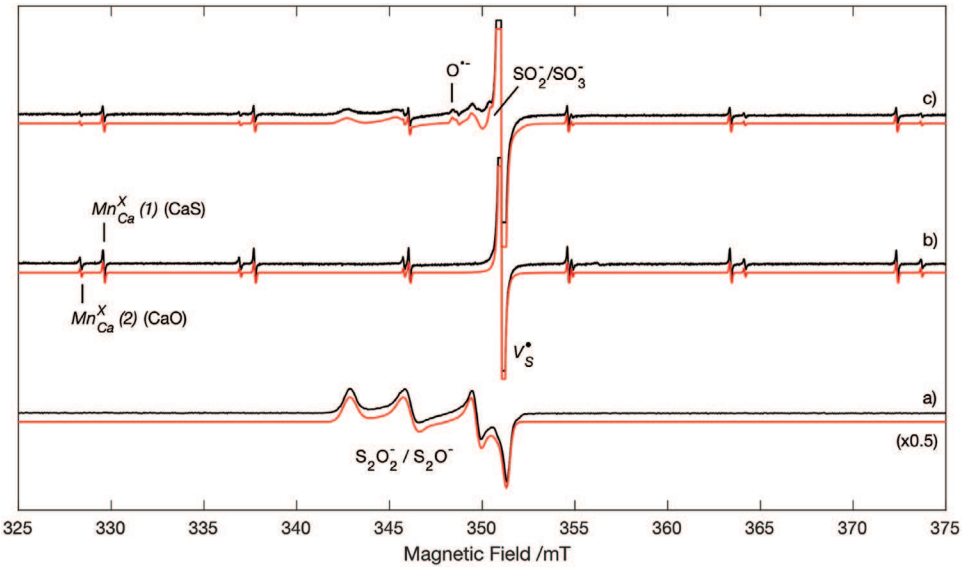


**Figure 3.** CW X-band (9 GHz) EPR spectra (120 K) of a) undoped CaS sample (see Figure S8 in the Supporting Information for simulation breakdown), and the same sample after treatment including b) heated to 973 K in $N_2/H_2$ and c) cryo-milled sample from (b) (see Figure S10, Supporting Information for simulation breakdown). The $V_S^{\bullet}$ signal in (b,c) is clipped for better resolution of weak signals. Black: experimental spectrum; Red: total simulated spectrum.

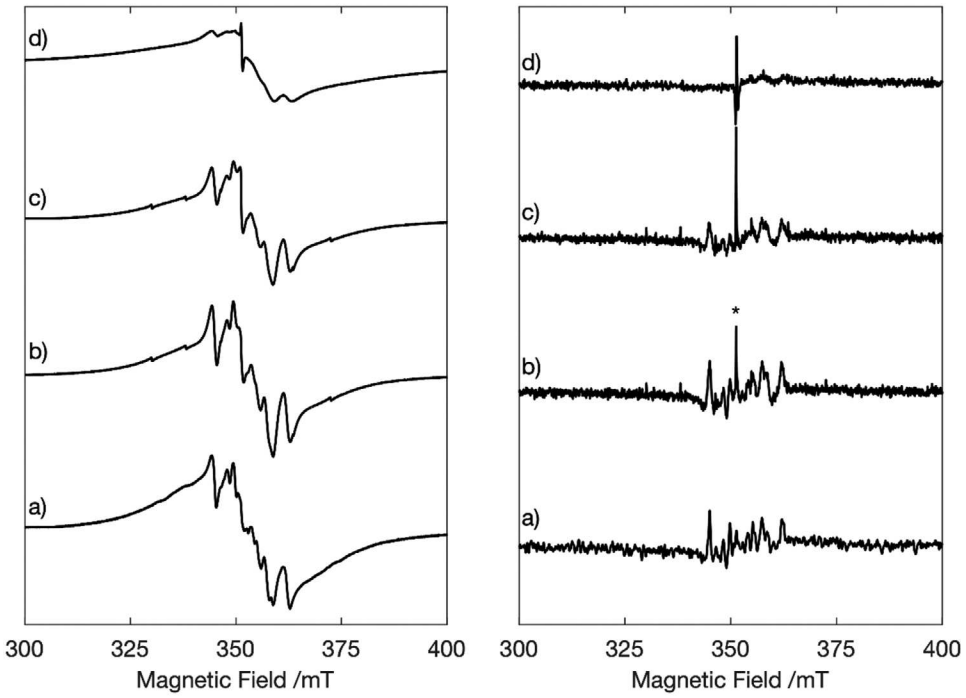


**Figure 4.** CW X-band (9 GHz) EPR spectra (120 K) of a) the native CaSEu_Na sample, after b) one (CaSEu_Na_C1), c) two (CaSEu_Na_C2), and d) three (CaSEu_Na_C3) consecutive cryo-milling treatments. Left: Standard first derivative measurements; Right: second derivative measurements indicating onset of $V_S^{\bullet}$ center signal, labeled by an asterisk.

into paramagnetic sulfur-oxygen based radicals. Another weak signal also appears to the low field of the $V_S^{\bullet}$ signal, as discussed below.

The extracted spin Hamiltonian parameters for distinct species in the native undoped sample, CaS_1, and after heating at 500 °C, may be compared to the complex spectrum observed in CaS_3. Most of the weakly resolved features, at low field of the $V_S^{\bullet}$ center, may now be identified as a mixture of $S_2O^-$ and $S_2O_2^-$ species, after partial oxidation of the buried diamagnetic $S^{2-}$ centers indicated vide infra (see Figure S9, Supporting Information). In addition, another unidentified species is also present at a field value of $B_0 = 334$ mT. The species appears to be characterized by an orthorhombic signal, with the $g$ values of 2.0167, 2.0184, and 2.0025, and can be tentatively assigned to a trapped hole center, generated by heat treatment.[15] It is reported that these defects can be stabilized by cations such as $Na^+$ which could be present as impurities, but cannot be detected directly using CW EPR.[15]

### 2.5. Cryo-Milling Study of Prepared CaS:Eu(Na) Sample

To determine the effect of local disorder in the sample upon cryo-milling, and to identify the presence of any intrinsic $V_S^{\bullet}$ centers in the doped sample, a systematic study of the effects of consecutive cryo-milling cycles on the samples was performed. Therefore, a CaS:Eu sample, prepared via a solid-state reduction method using a carbon reductant and source of $Na^+$ impurities, was used in order to manipulate the redox state of $Eu^{2+}$ in the sample via charge compensation and thus reduce the signal intensity. This sample has been labelled as CaSEu_Na and the subsequent cryo-milled samples CaSEu_Na_C$x$ ($x$ = 1,2,3) respectively where $x$ is the number of consecutive cycles.

**Figure 4** presents the X-band CW EPR spectra of this CaSEu_Na sample, after one, two and three consecutive cycles. For clarity, the spectra are shown in first and second derivative mode. In the native sample, a hyperfine pattern indicative of the isolated $Eu^{2+}$ species is observed (Figure 4a), similar to the commercial samples discussed earlier (Figure 1a). After the first cryo-milling cycle (Figure 4b), an increase in $Eu_{Ca}^{x}$ signal intensity is observed which is attributed to reduction of the unreacted Eu precursor and carbon reductant. In the second derivative mode, an additional sharp isotropic signal is clearly observed with $g = 2.0031$ and which can be attributed to the $V_S^{\bullet}$ center. After an additional cryo-milling cycle (Figure 4c), the $Eu_{Ca}^{x}$ signal decreases further, presumably due to oxidation to $Eu_{Ca}^{\bullet}$, while simultaneously the $V_S^{\bullet}$ center signal intensity increases. In the first derivative spectrum, a change in the line shape within the $Eu_{Ca}^{x}$ hyperfine multiplet indicates the appearance of the $V_S^{\bullet}$ center signal which was not resolved. Finally, after the third consecutive cryo-milling cycle (Figure 4d), the $Eu_{Ca}^{x}$ concentration reduces further, accompanied by a significant broadening in the linewidth. This change to the linewidth is likely due to the increased spin concentration around the $Eu_{Ca}^{x}$ site, which reduces the $T_2$ relaxation time and thereby increases the homogeneous linewidth contribution. Additional strain effects, such as distribution of the $b_4$ terms included in the broadening model, due to disorder within the sample, is also likely to contribute to the broadening.

### 2.6. XPS Studies of Commercial and Prepared CaS:Eu Phosphors

In order to provide a comparison between the distinct paramagnetic $Eu^{2+}$ environments as identified by EPR, additional XPS measurements were performed on the commercial treated samples CaSEu_1, 2 and 3, as well as the solid-state reduced sample CaSEu_SSR. The Eu 3d XPS region is shown for these four samples in **Figure 5**.

For the treated commercial samples, CaSEu_1, 2, and 3, no well resolved signals were observed in the Eu 3d region for either $Eu^{2+}$ or $Eu^{3+}$, indicating Eu is either below the limits of detection, or absent from the surface region, and are therefore distributed within the bulk of the material as expected from the EPR data. However, for CaSEu_SSR, Figure 5d, broad peaks were observed at binding energies of 1134.6 and 1164.6 eV along with weakly resolved satellite features, which correspond to the Eu $3d_{5/2}$ and $3d_{3/2}$ regions typical of oxygen containing $Eu^{3+}$ species.[28] The binding energies of the observed signals are comparable to those reported for $Eu(OH)_3$, present at 1134.4 and 1164.2 eV for the $3d_{5/2}$ and $3d_{3/2}$ regions respectively.[29] The binding energies for $Eu^{2+}$, the EPR-active state, are typically reported to be around 1125 and 1155 eV for the $3d_{5/2}$ and $3d_{3/2}$ core levels[30,31] and would be well removed from the observed spectral lines. We can therefore be confident that the XPS signals do not directly correspond to paramagnetic $Eu^{2+}$ (within the limits of detection). By comparison to the native sample, CaSEu_1, these broad peaks are also observed to be very weakly resolved from the baseline.

In the O 1s region, a major peak was observed in all samples at 531.4 eV which was attributed to a CaO or $CaSO_4$ type phase (O 1s binding energy reported as 531.2 eV for CaO and 531.5 eV for $CaSO_4$)[32] resulting from the oxidation of CaS, The line shape and peak height is not observed to change significantly upon treatment of the sample from CaSEu_1 to 3. The presence of these phases was also evidenced by the spin Hamiltonian parameters for the $Mn^{2+}$ impurity for the undoped samples CaS_2 and CaS_3. For CaSEu_SSR, an asymmetry is evident to higher binding energy of the larger peak observed in all samples, corresponding to the presence of another distinct signal at 533.1 eV. This could indicate a surface hydroxyl species, such as that attributed to the broad Eu 3d signal and has been tentatively assigned to $Eu(OH)_3$. Such adsorbed hydroxyl species have been reported in $Eu_2O_3$ host materials (532.7 eV).[33]

The findings reported for the Eu 3d and O 1s regions of the CaSEu_SSR sample indicate that Eu is present at the surface, which has not been successfully doped into the material. This indirectly corroborates to the observation of a low symmetry $Eu^{2+}$ species from W-band EPR measurements of CaSEu_SSR and CaSEu_1, which was attributed to the $Eu^{X}_{surface}$ species in an "EuO" type phase, for which the exact composition was not determined.

The Ca and S 2p regions for all samples (see Figures S12 and S13, Supporting Information) consisted of multiple signals expected to relate to various phases containing Ca, S, and O. The similarity of the binding energies, and lack of corroborating literature values, was not conclusive of any significant findings with respect to the characterization of the luminescent $Eu^{2+}$ environments.

### 2.7. Luminescence Studies of CaS:Eu Phosphors

The photoluminescent properties of the different phosphors were also assessed using steady state luminescence

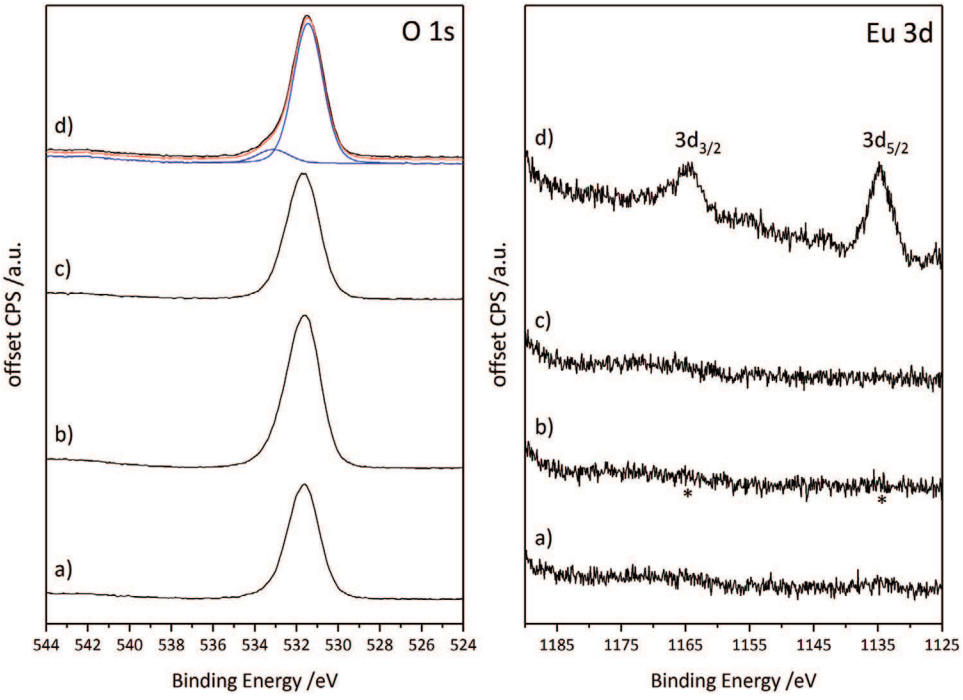


**Figure 5.** XPS spectra for commercial CaSEu_1, 2, and 3 samples, compared to the sample prepared via solid state reduction method (CaSEu_SSR). Experimental traces are shown in black. Left: O 1s region with simulations for CaSEu_SSR. Red trace = simulation envelope; Blue traces = simulation components. Right: Eu 3d region. See Figure S11 in the Supporting Information for survey spectra.

spectroscopy on solid samples. Since the characteristic phosphorescence emission wavelengths of $Eu^{3+}$ are likely to overlap with the broad emission spectrum that is typically attributed to the $Eu^{2+}$ doped phosphor species, it can be challenging to establish the presence of a $Eu^{3+}$ contaminant/by-product in such species. Therefore, the photophysical properties of the different samples were investigated using a range of excitation wavelengths. In particular, the possibility that $Eu^{3+}$ may be present in the samples was interrogated using an excitation wavelength of 395 nm, as this provides direct promotion of the spin forbidden $^7F_0 \rightarrow {}^5L_6$ transition, which can then rapidly relax to the emitting $^5D_0$ excited state of $Eu^{3+}$.

First, all samples were investigated using an excitation wavelength of 250 nm and displayed the expected broad emission peak peaking around 640 nm, which is consistent with the previously reported $Eu^{2+}$-based (5d–4f transition) emission that is commonly observed for this class of $Eu^{2+}$-doped phosphor (**Figure 6**, left). The excitation acquisition ($\lambda_{em}$ = 645 nm) revealed a longest wavelength feature at 450–550 nm. When analyzing sample CaS:Eu_Na_C3 (after 3 cryo-milling cycles) this emission feature, although present, appeared to be much weaker. In addition, weak shorter wavelength emission bands between 300 and 550 nm were also noted although these were absent in all other samples.

Each of the samples was also investigated using an excitation wavelength of 395 nm. In only one case, CaSEu_Na_C3, was the broad 645 nm peak not observed. Instead, we noted a very weak set of peaks superimposed upon the tail of a shorter wavelength emission feature (Figure 6, right). These weaker bands were consistent with the luminescence spectroscopic signature of $Eu^{3+}$: from this spectrum there was unequivocal evidence for the $^5D_0 \rightarrow {}^7F_J$ transitions at around 590 nm, 615 nm and 700 nm (for $J = 1$, $J = 2$ and $J = 4$, respectively). A corresponding excitation spectrum ($\lambda_{em}$ = 592 nm) also revealed a weak, but sharply distinctive band at 395 nm again corroborating the assignment of these features to the presence of $Eu^{3+}$ in the sample. Therefore, the third consecutive cryo-milling cycle not only reduced the $Eu^{2+}$ concentration but was also accompanied by an increased concentration of $Eu^{3+}$, due to an oxidative process, which was not possible to detect directly using EPR characterization due to its singlet ground state.

## 3. Conclusion

In conclusion, EPR investigations supported by XPS and photoluminescence measurements have been utilized in order to better understand the nature of local $Eu^{2+}$ sites, defects, and impurities in CaS:Eu red-emitting phosphors. The effect of synthetic and post-synthetic treatments was also rationalized in terms of activating and deactivating species that directly affect the luminescent properties. EPR measurements of the native sample showed a complex hyperfine structure at $g < g_e$ indicative of a well isolated $Eu^{2+}$ site, $Eu^{X}_{Ca}$, located in a cubic substitutional site ($Ca^{2+}$). Upon treatment, $Mn^{2+}$ impurities, $Mn^{X}_{Ca}$, became evident which are expected to be present also in substitutional $Ca^{2+}$ sites. The $Eu^{X}_{Ca}$ signal intensity was also observed to decrease following oxidation to $Eu^{3+}$, $Eu^{\cdot}_{Ca}$. Upon application of heating treatment, the signal intensity was partially improved and the change in line shape of $Mn^{X}_{Ca}(1)$ is indicative in the change of local order within the cubic lattice due to unresolved fine structure. $F^+$ center defects, $V_S^{\cdot}$, were observed

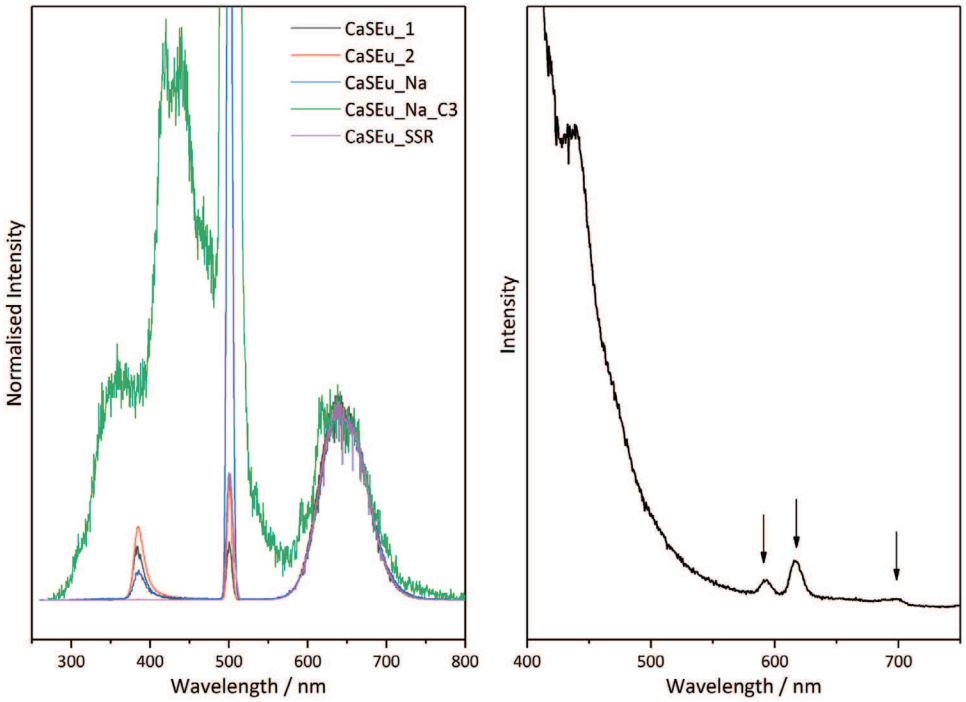


**Figure 6.** Left: A comparison of the emission spectra of the samples using $\lambda_{ex}$ = 250 nm (note double harmonic feature at 500 nm), normalized to the intensity of the peak around 645nm; Right: The emission spectra of CaSEu_Na_C3 obtained using $\lambda_{ex}$ = 395 nm. The arrows indicate the $Eu^{3+}$ centered $^5D_0 \rightarrow {}^7F_J$ transitions where $J = 1$, $J = 2$ and $J = 4$.

in the prepared undoped materials, and also after several cryo-milling cycles, which are well known to reduce the efficacy of the material. In the prepared CaSEu_SSR sample, W-band EPR measurements and XPS indicated the presence of an additional "EuO" type surface species, $Eu^{X}_{surface}$, not incorporated into the lattice, which was also weakly resolved in the W-band measurements of the native commercial sample, CaSEu_1. This species is responsible for the fine structure not observed within the simulations for the $Eu^{X}_{Ca}$ site. Finally, the findings from EPR measurements were rationalized using photoluminescence spectroscopy to give a qualitative account of their effect on the luminescent properties. The outcomes of this work demonstrate the utility of EPR, in addition to complementary spectroscopic techniques, in the design and development of better performing materials for specific application.

## 4. Experimental Section

*Materials*: The commercial sample, CaS:Eu in its native form (CaSEu_1) was purchased from Phosphor Technologies Ltd. and used as received without further purification or treatment.

*Sample Preparation—Coprecipitation Method for Undoped Samples*: The procedure used for the preparation of the undoped samples was modified from a method previously reported by Rekha et al.[34] who used 2-propanol as the solvent. Solution A was prepared by dissolving anhydrous CaCl2 (3.077 g, 28 mmol) in 56 mL of ethanol. Nitrogen was then bubbled continuously through the solution. Solution B was prepared by dissolving anhydrous $Na_2S$ (2.164 g, 28 mmol) in 56 mL of ethanol. A yellow, slightly cloudy solution resulted. Solution B was then added dropwise over 10 min to solution A with stirring to form a white suspension.

This suspension was warmed to approximately 60 °C and left stirring overnight with nitrogen bubbling to produce a faintly yellow fine powder. This powder was then transferred quickly under nitrogen to an alumina boat in a tube furnace previously flushed with $N_2$/2% $H_2$ and left under this gas for several hours. The sample was then annealed at 700 °C (10 °C $min^{-1}$ ramp up, dwell 2 h, 20 °C $min^{-1}$ to R.T.).

*Sample Preparation—Solid State Reduction Method for Doped Samples*: The method used was that described by Hubacek et al.[35] Urea (45 g 0.749 mol) was mixed with $CaSO_4$ (6 g, 44.07 mmol) and $Eu(NO_3)_3{\cdot}6H_2O$ (0.22 g 0.651 mmol) and initially heated in an open alumina crucible on a hot plate to 150 °C where the mixture became liquid. The mixture was then stirred briefly, and the temperature raised. At 160 °C, gas evolution was seen to occur. After an hour at ≈200 °C, solidification occurred, A white lumpy product was obtained, which was easily crushed to a powder. The product was ground with a pestle and mortar and heated to 550 °C (30 min, 30 min, 20 min) in a loosely covered crucible in air. the powder was then heat-treated at 700 °C under 5% $H_2/N_2$ (10 °C $min^{-1}$ ramp up, 120 min dwell, 20 °C $min^{-1}$ ramp down). A very pale pink product was obtained. This was only weakly fluorescent under long wave UV (pinky bluish white), but quite strongly red under short wave UV irradiation.

*Solid State Reduction Method for CaSEu_Na*: The Na co-doped sample was prepared via a method similar to that previously reported by Guo et al.[36] A flux composed of $CaSO_4$ (25.21 g, 0.18 mol), $Na_2S_2O_3$ (4.40 g 27.8 mmol), $Eu(NO_3)_2{\cdot}5H_2O$ (0.59 g, 1.37 mmol) and a carbon black reductant (4.38 g, 0.364 mol) were mixed in a planetary ball mixer with ceramic beads for 30 min to obtain a well-mixed powder. The powder was sieved, packed into a ceramic crucible and covered with a graphite foam to limit oxidation of the sample. The crucible was subsequently fired at 950 °C, with a 20 °C $min^{-1}$ ramp rate, for 2 h before leaving overnight to cool. The sample was obtained as a black powder due to residual carbon. A red emission was observed under a UV torch confirming the presence of luminescent $Eu^{2+}$ sites and the sample was used without further treatment.

*Sample Treatments—Cryomilling Treatment*: The samples CaSEu_1, CaS_2, and CaSEu_Na were milled in a Retsch Cryo-mill with an initial 8 min cooling stage at 5 Hz. This was followed by three consecutive milling stages at 30 Hz, with interstage cooling periods of 3 min at 5 Hz to normalize any temperature increase from the grinding action.

*Sample Treatments—Heating Treatment in Air and $N_2/H_2$*: For heating treatments in $N_2/H_2$, the samples were treated as described in the co-precipitation synthesis method. For heat treatments in air, the sample was contained in an alumina boat and placed into a Nannetti fast-fire furnace for a dwell time of 30 min.

*Characterization Techniques—CW EPR Spectroscopy*: The samples for EPR measurements were used either as prepared or as received, and ≈50 mg of the powders were packed into a standard 4 mm quartz tube. The X-band (9 GHz) CW-EPR spectra were recorded at 140 K on a Bruker EMX spectrometer, and unless otherwise stated, operating at 100 kHz field modulation frequency; 2 mW microwave power; 1 G modulation amplitude using an ER 4119HS cavity. For W-band measurements, the samples were packed in a 0.5 mm I.D. quartz cell The W-band (95 GHz) CW-EPR spectra were recorded at 300 K on a Bruker E600 spectrometer operating at 100 kHz field modulation frequency; 0.005 mW microwave power; 1 G modulation amplitude, using a E600-1021H TeraFlex resonator. Field calibration was performed using a BDPA standard at X-band, and the microwave frequency for spectra at W-band were adjusted accordingly by simultaneous fitting at the two microwave frequencies. Spectral simulations were performed using the EasySpin toolbox in MATLAB developed at ETH Zurich.[37] The second derivative spectra in Figure 4 were smoothed using a spline modelling approach with the MATLAB curve fitting toolbox to improve the signal resolution.

*Characterization Techniques—X-Ray Photoelectron (XPS) Spectroscopy*: A Kratos Axis Ultra DLD system was used to collect XPS spectra using monochromatic Al Ka X-ray source operating at 120 W (10 mA × 12 kV). Data were collected with pass energies of 160 eV for survey spectra, and 20 eV for the high-resolution scans with step sizes of 1 and 0.1 eV, respectively. The system was operated in the hybrid mode of operation utilizing a combination of magnetic and electrostatic lenses for electron collection over an analysis area of ≈300 × 700 $\mu m^2$. A magnetically confined electron-only charge compensation system was used to minimize charging of the sample surface, and all spectra were taken with a 90° take off angle. A pressure of $\approx 1 \times 10^{-9}$ Torr was maintained during collection of the spectra, with base pressure of the system $5 \times 10^{-10}$ Torr. All data were calibrated to the C(1s) line of adventitious carbon, taken to have a value of 284.8 eV, and quantified using CasaXPS (v2.3.23) using modified Wagner sensitivity factors as supplied by the manufacturer, after subtraction of a two parameter Tougaard background defined as a "U2 Tougaard" background in the analysis software.

*Characterization Techniques—Photoluminescence Spectroscopy*: All photophysical data were obtained on a Jobin-Yvon Horiba Fluorolog-3 spectrometer fitted with a JY TBX picosecond photodetection module. Solid samples were used in all cases and a front face accessory was used for light collection. Emission spectra were uncorrected and excitation spectra were instrument corrected.

## Supporting Information

Supporting Information is available from the Wiley Online Library or from the author. The dataset file associated with this work may be accessed using the following link: http://doi.org/10.17035/d.2020.0115658963.

## Acknowledgements

The authors thank the EPSRC and Johnson Matthey for funding JS (through an iCASE award) and EPSRC for the grant EP/P019951. XPS data collection was performed at the Cardiff hub of the EPSRC National Facility for XPS ("HarwellXPS"), operated by Cardiff University and UCL, under contract No. PR16195. The manuscript was written with contributions from all authors. All authors have given approval to the final version of the manuscript.

## Conflict of Interest

The authors declare no conflict of interest.

## Keywords

electron paramagnetic resonance, europium, luminescence, phosphors, X-ray photoelectron spectroscopy

Received: July 22, 2020
Revised: August 16, 2020
Published online: September 9, 2020

[1] Y. Zhang, J. Hao, *J. Mater. Chem. C* **2013**, *1*, 5607.
[2] A. de Bettencourt-Dias, *Dalton Trans.* **2007**, *0*, 2229.
[3] Y. Lu, B. Yan, *Chem. Commun.* **2014**, *50*, 15443.
[4] K. Van den Eeckhout, P. F. Smet, D. Poelman, *Materials* **2010**, *3*, 2536.
[5] Y. Liang, F. Liu, Y. Chen, X. Wang, K. Sun, Z. Pan, *J. Mater. Chem. C* **2017**, *5*, 6488.
[6] P. Dorenbos, R. Visser, C. W. E. van Eijk, N. M. Khaidukov, M. V. Korzhik, *IEEE Trans. Nucl. Sci.* **1993**, *40*, 388.
[7] C. W. E. van Eijk, *Nucl. Instrum. Methods Phys. Res., Sect. A* **1997**, *392*, 285.
[8] C. W. E. van Eijk, *Phys. Med. Biol.* **2002**, *47*, R85.
[9] V. B. Pawade, H. C. Swart, S. J. Dhoble, *Renewable Sustainable Energy Rev.* **2015**, *52*, 596.
[10] J. Garcia, M. J. Allen, *Eur. J. Inorg. Chem.* **2012**, *2012*, 4550.
[11] X. Qin, X. Liu, W. Huang, M. Bettinelli, X. Liu, *Chem. Rev.* **2017**, *117*, 4488.
[12] D. Caurant, D. Gourier, N. Demoncy, I. Ronot, J. Pham-Thi, *J. Appl. Phys.* **1995**, *78*, 876.
[13] R. L. Nyenge, H. C. Swart, O. M. Ntwaeaborwa, *Opt. Mater.* **2015**, *40*, 68.
[14] R. D. Shannon, *Acta Crystallogr., Sect. A: Found. Adv.* **1976**, *32*, 751.
[15] D. Caurant, D. Gourier, N. Demoncy, M. Pham-thi, *Radiat. Eff. Defects Solids* **1995**, *135*, 115.
[16] P. K. Ghosh, R. Pandey, *J. Phys. C: Solid State Phys.* **1982**, *15*, 5875.
[17] R. Pandey, A. B. Kunz, J. M. Vail, *J. Mater. Res.* **1988**, *3*, 1362.
[18] P. K. Ghosh, H. P. Narang, H. Chander, *J. Lumin.* **1986**, *35*, 99.
[19] *Electron Paramagnetic Resonance*, Vol. *26* (Eds: V. Chechik, D. M. Murphy; book series:, SPR - Electron Paramagnetic Resonance), The Royal Society of Chemistry, London **2019**.
[20] N. J. Stone, *Table of Nuclear Magnetic Dipole and Electric Quadrupole Moments, IAEA Nuclear Data Services*, International Atomic Energy Agency, Vienna, Austria **2011**.
[21] J. W. Jewett, P. E. Wigen, *J. Chem. Phys.* **1974**, *61*, 2991.
[22] N. Sabbatini, M. Ciano, S. Dellonte, A. Bonazzi, F. Bolletta, V. Balzani, *J. Phys. Chem.* **1984**, *88*, 1534.
[23] A. Abragam, B. Bleaney, *Electron Paramagnetic Resonance of Transition Ions* (Oxford Classic Texts in the Physical Sciences), Oxford University Press, Oxford **2012**.
[24] R. Boča, *Coord. Chem. Rev.* **2004**, *248*, 757.
[25] İ. Yildirim, B. Karabulut, E. Bozkurt, F. Köksal, *Radiat. Phys. Chem.* **2009**, *78*, 165.
[26] J. Rubio O., E. Muñoz P., J. Boldú O., Y. Chen, M. M. Abraham, *J. Chem. Phys.* **1979**, *70*, 633.
[27] B. Ray, P. A. M. Mirzai, J. W. Brightwell, *Phys. Status Solidi A* **1987**, *100*, 233.
[28] Y. Uwamino, T. Ishizuka, H. Yamatera, *J. Electron Spectrosc. Relat. Phenom.* **1984**, *34*, 67.
[29] P. Li, H. Wu, J. Liang, Z. Yin, D. Pan, Q. Fan, D. Xu, W. Wu, *Radiochim. Acta* **2017**, *105*, 1049.
[30] R. Vercaemst, D. Poelman, L. Fiermans, R. L. Van Meirhaeghe, W. H. Laflère, F. Cardon, *J. Electron Spectrosc. Relat. Phenom.* **1995**, *74*, 45.
[31] T. Maruyama, S. Morishima, H. Bang, K. Akimoto, Y. Nanishi, *J. Cryst. Growth* **2002**, *237-239*, 1167.
[32] C. D. Wagner, D. A. Zatko, R. H. Raymond, *Anal. Chem.* **1980**, *52*, 1445.
[33] J. P. Baltrus, M. J. Keller, *Surf. Sci. Spectra* **2019**, *26*, 014001.
[34] S. Rekha, A. I. Martinez, T. A. Safeera, E. I. Anila, *J. Lumin.* **2017**, *190*, 94.
[35] M. Hubacek, K. Takahashi, *US 7378038*, **2008**.
[36] C. Guo, D. Huang, Q. Su, *Mater. Sci. Eng., B* **2006**, *130*, 189.
[37] S. Stoll, A. Schweiger, *J. Magn. Reson.* **2006**, *178*, 42.